Control Engineering Practice 170 (2026) 106805

Contents lists available at ScienceDirect

Control Engineering Practice

journal homepage: www.elsevier.com/locate/conengprac

# Electrically actuated control system for the stabilization of synchrotron X-ray beams

Niccolò La Rosa [a,b,*], Samuele Moscato [a,b], Luigi Fortuna [b], Maide Bucolo [a,b], Massimo Camarda [a,b,c,d]

[a] Università degli Studi di Catania, Via Santa Sofia, 64, Catania, 95123, Italy
[b] STLab s.r.l, Via Anapo, 53, Catania, 95126, Italy
[c] SenSiC GmbH, Switzerland Innovation Park Innovaare, Villigen, Switzerland
[d] CNR-IMM, Ottava strada, 5, Catania, 95121, Italy

ARTICLE INFO

*Keywords:*
X-ray diagnostic
Fast orbit feedback
XBPM
PID controls

ABSTRACT

Maintaining sub-micrometer stability of synchrotron X-ray beams is essential for the accuracy and repeatability of cutting-edge scientific and medical experiments. Traditional beamline stabilization systems, based on mechanical actuation of optical elements, are inherently limited in speed due to physical constraints like friction and inertia. This study introduces an innovative control strategy based on electrical actuation, directly influencing the bending magnet responsible for steering the beam into the beamline. This approach unlocks the potential for significantly higher control frequencies, comparable to those used for the electron beam stabilization. A laboratory-scale replica was developed to validate the feasibility and robustness of this method. A Proportional-Integral (PI) controller has been implemented to stabilize the electron beam and compensate for disturbances. Experimental results demonstrate that this strategy enables precise, high-frequency beam stabilization, even in the presence of typical disturbances such as position drift occurring during X-Ray Absorption Spectroscopy (XAS) experiments. This work lays the groundwork for next-generation control systems in synchrotron facilities, aiming to enhance performance and open the door to more advanced experimental capabilities.

## 1. Introduction

Synchrotron accelerators are well-established facilities widely used in various fields of scientific research and medical applications, including physics, materials science, biology, and medicine. In particular, synchrotron radiation sources play a crucial role in numerous biomedical applications due to their unique characteristics, such as high intensity, spatial and temporal coherence, brilliance, and a broad radiation spectrum covering wavelengths from infrared to X-rays (Fan & Zhao, 2018; Möller, 2020).

The main components of a synchrotron light source station are highlighted in Fig. 1(a), where the following elements can be identified: (i) Electron source (e-GUN), which generates the initial electron beam, (ii) Linear accelerator (LINAC), which accelerates the beam to hundreds of $MeV$, (iii) Booster ring, further accelerating the electron to final energies ranging from 100 $MeV$ to 6 − 7 $GeV$, (iv) Storage ring, which maintains the accelerated electrons in a stable circular path, (v) Insertion devices, which convert a portion of the electron beam's energy into polychromatic photon beams, known as synchrotron radiation, and (vi) beamlines, which are straight sections connected to the storage ring and located downstream of the insertion devices. Beamlines contain various components designed to manipulate and control the emitted radiation according to specific experimental needs.

The stabilization of X-ray beams in synchrotron beamlines is a crucial aspect to ensure high quality and repeatability of experimental measurements. The need to maintain beam stability within the sub-micrometer range (Rehm, 2013) imposes the adoption of advanced control systems. In fact, both the electron beam and the x-ray beam are subject to various disturbances, ranging from low-frequency effects, such as thermal drifts and magnets misalignment, to higher-frequency disturbances, reaching several hundred hertz, including mechanical vibrations (Wang et al., 2012) and electrical noise from power supplies (Huang et al., 2021).

To compensate for these disturbances, two types of control systems are currently in use: Global Orbit Feedback Systems (GOFB), which stabilize the electron beam within the ring, and Beamline Control Systems, which stabilize the x-ray beam in the beamline. The GOFB can be further divided into two components: Slow Orbit Feedback (SOFB) and Fast Orbit Feedback (FOFB). The SOFB is responsible for correcting

* Corresponding author.
*E-mail address:* niccolo.larosa@phd.unict.it (N. La Rosa).

https://doi.org/10.1016/j.conengprac.2026.106805
Received 7 July 2025; Received in revised form 24 December 2025; Accepted 20 January 2026
Available online 31 January 2026

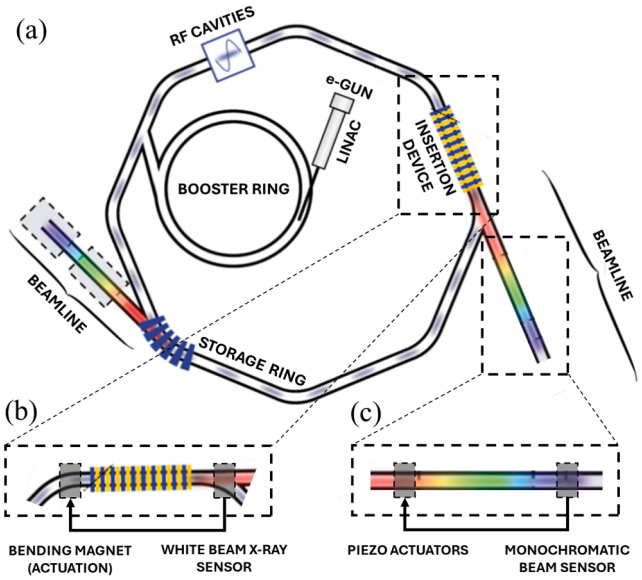


**Fig. 1.** (a) Overview of the main components of a synchrotron facility. (b) Details regarding the devices required to perform a control system utilizing electrical actuation: the bending magnet corrects the electron beam before it enters in insertion device, and the feedback is closed by a white beam x-ray sensor, placed downstream of the Insertion Device (ID). (c) Details regarding the state-of-the-art devices to perform beamline control: in this case, the x-ray beam position and intensity are controlled by elliptical cylindrical mirrors or monochromator directing, using piezo actuators; the feedback is closed by a monochromatic beam sensor placed before the beam enters the end station. (For interpretation of the references to color in this figure legend, the reader is referred to the web version of this article.)

low-frequency components, while the FOFB acts on high-frequency disturbances. For example, at the SOLEIL synchrotron, the SOFB and FOFB operate together to compensate for disturbances in a frequency spectrum from Direct Current (DC) to 250 $Hz$, monitoring the position of the electron beam through a set of 120 Beam Position Monitors (BPMs) (Forck et al., 2009) distributed along the storage ring, each equipped with a dedicated Field-Programmable Gate Array (FPGA) for integrating the Proportional-Integral-Derivative (PID) based control algorithm (Engblom et al., 2016; Hubert et al., 2016, 2009). At the National Synchrotron Light Source (NSLS-II), thanks to a precise identification of the process transfer function (Kongtawong et al., 2020) and a control architecture, also FPGA-based but more centralized (Tian et al., 2015), a closed-loop gain bandwidth of 400 $Hz$ and 300 $Hz$ has been achieved in the horizontal and vertical planes, respectively.

In addition to GOFB, local control on beamlines is equally crucial to ensure that the X-ray beam remains stable at the experiment's impact point, allowing for compensation of residual disturbances from the ring, but also of other disturbances introduced by local vibrations or during specific experiments, such as position drifts during X-ray Absorption Spectroscopy (XAS) experiments, caused by monochromator misalignment (Bai et al., 2023). For example, at the Shanghai Synchrotron Radiation Facility (SSRF), an automatic feedback system was implemented for beamline BL08U1A, which, through a control algorithm integrated into Experimental Physics and Industrial Control System (EPICS), allowed optimal beam flux to be achieved (Zhang et al., 2023). Also, in the same station, a dual-frequency PID-based feedback system was implemented within beamline BL13U to control, through a single position signal extrapolated from an X-ray Beam Position Monitors (XBPM), a deflection mirror and a Double Crystal Monochromator (DCM) at different frequencies (Jiang et al., 2025). At the National Synchrotron Light Source (NSLS-II), a control system was implemented to stabilize the beam along the FMX and AMX beamlines, consisting of three feedback loops: the first acting directly on the electron beam at the beamline entrance, and the remaining two acting on the X-ray beam to control it through piezo motors that move the double crystal monochromator and the focusing mirrors present in the beamlines (Schneider et al., 2021). Moreover, control systems specifically designed for the management of X-ray beams are available on the market, such as the B.E.S.T. system sold by CAEN ELS (ELS, 2025). Even with the presence of sophisticated hardware, such as FPGAs, these control systems achieve lower frequencies than the GOFB, as they are limited by the mechanical constraints-primarily friction and inertia-of the optical elements being controlled. As a result, the control frequencies typically reach only the order of tens of hertz. In this context, significant progress has been made with piezo-actuated adaptive x-ray optics (e.g., bimorph/deformable mirrors), which improve local beam stability but remain ultimately bandwidth-limited by mechanical inertia and high-voltage driver dynamics (Alcock et al., 2018; Huang et al., 2016). To address this limitation, the solution proposed in this study is the development of a control system that no longer acts on the beamline's optical elements-i.e., a mechanically actuated approach-but instead acts on the bending magnet that steers the beam toward the beamline. This electrically actuated strategy, described in Fig. 1(b) could enable significantly higher control frequencies, potentially reaching the same order as those of the GOFB. Indeed, recent work at Diamond Light Source (DLS) (Bloomer et al., 2019) has investigated implementing a feedback system that steers the electron beam upstream of the insertion device (ID) using photon-beam position measurements downstream of the ID. The results demonstrate beam-stability improvements with closed-loop bandwidths exceeding 1 kHz, a regime generally inaccessible to conventional mechanically actuated systems. The key challenge in this approach is to demonstrate that the bending magnet can serve as an effective actuator for stabilizing the radiation beam within the beamline, without compromising the stability of the electron beam inside the storage ring. Given the difficulties and high costs of having direct and continuous access to a synchrotron or LINACS beam, it was deemed preferable to identify a process with dynamics sufficiently comparable to those of the electron beam in the synchrotron, to recreate a laboratory-scale replica of the real case study.

In this context, we designed and implemented a cost-effective lab-replica, based on an analog oscilloscope, capable of reproducing the main features of a beamline at zero operational cost. In this setup, the process to be controlled is the spot position on the oscilloscope screen. Its displacement is monitored by a Beam Position Monitor (BPM) operating in the visible range, which relies on the same principle as the X-ray BPMs used in synchrotron facilities, while the actuation is performed electrically through the oscilloscope's deflection magnets. The process was modeled and characterized, and a PI control system was first validated in simulation and then implemented on a microcontroller. Experimental tests demonstrated that the system can effectively stabilize the beam, both in noise-free and noisy conditions, and even under disturbances emulating those induced by XAS experiments.

The paper is organized as follows. Sections 2.1 and 2.2 introduce the Lab-Replica oscilloscope-based development and the system architecture. Sections 2.3 and 2.4 describe the model identification methodology and the related results. In Section 3, the adopted control strategy is presented. In Section 4, the obtained control loop performances are presented. Finally, discussion and future works are described in Section 5.

## 2. Lab-replica beam position model

### 2.1. Lab-replica system realization

The replica was developed using the setup presented in Fig. 2, explained in more detail in the following:

- The main block is an oscilloscope (i.e., the beam source replica) that represents the process to be controlled. It serves to replicate the real case actuation system, specifically the deflection magnets

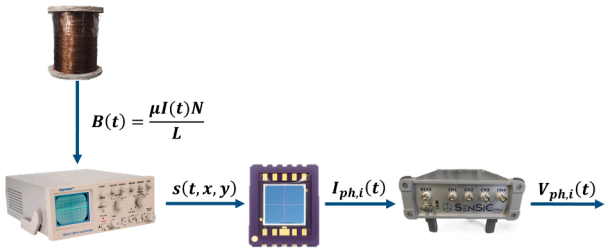


**Fig. 2.** Block diagram of the devices used for the synchrotron Lab-Replica. From left to right: The analog oscilloscope is used as the electron beam source; the electromagnet is used as a disturbance source, deflecting the electron beam by the generation of a time-variable magnetic field; the $2 \times 2$ photodiode matrix is used to detect the spot position on the oscilloscope screen; the picoammeter serves as a current readout system.

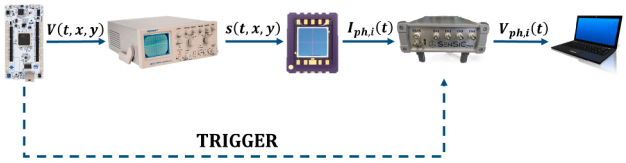


**Fig. 3.** Open-loop system used for the identification of the lab-replica mathematical model. Compared to Fig. 2, the STM32-H723ZG microcontroller has been added, as it is responsible for generating the control voltages that move the spot along the $x$ and $y$ axes. The microcontroller applies two voltage levels to the oscilloscope's probes, and the resulting spot position is encoded in 4 voltage values, read by the picoammeter and transmitted to the Personal Computer (PC) via serial communication. To ensure synchronization between the input voltages generated by the microcontroller and the data acquisition from the picoammeter, a trigger signal is enabled between the two devices.

placed upstream of the undulator. The oscilloscope operates by generating an electron beam within its Cathode Ray Tube (CRT), focused and manipulated using two components known as *deflection plates*. The output signal $s(t, x, y)$ is expressed as a Gaussian distribution function of the beam intensity, where the variables $(x, y)$ represent the horizontal and vertical coordinates on the oscilloscope screen, corresponding to the position of the luminous spot generated by the electron beam on the CRT plane.

- An electromagnet, placed on top of the oscilloscope, is used as a disturbance source. It consists of 800 windings, an inductance $L = 0.31\ H$, and a cutoff frequency of 500 $Hz$. The generated magnetic field $B(t)$ interacts with the beam, changing its position.
- To replicate the electronics used for beam monitoring within the synchrotron, an optical sensor composed of a $2 \times 2$ photodiode matrix, geometrically equivalent to the XBPM state-of-the-art sensor (Bloomer & Rehm, 2016), was employed. In this case, since the electron beam from the oscilloscope strikes a phosphor-coated screen and becomes fluorescent, the sensor was selected to be sensitive to the wavelength of the emitted light (approximately 565 $nm$, corresponding to green light). The intensity distribution of the light-spot $s(x, y)$ is measured by the detector, generating four output currents $I_{ph,i}(t)$, one for each sensor quadrant, proportional to the intensity of the detected light.
- To measure the currents generated by the sensor, the PCR4 picoammeter, marketed by SenSic, was used (SenSic, 2024). This instrument is specifically designed for high-speed digital multichannel low-current measurements, with typical applications including the readout of 4-quadrant photodiodes used for real-time monitoring of X-ray beams in synchrotrons and Free Electron Lasers (XFELs). The device features four trans-impedance input stages for current sensing, which allow the measurement of bipolar current ranging from $\pm 25\ nA$ to $\pm 50\ mA$. As a standard approach, throughout all experimental campaigns, the trans-impedance stage capable of enabling the measurement of bipolar currents ranging from $\pm 2.5\ \mu A$ was employed. The output currents are measured by the device, with certain accuracy, and converted into voltages $V_{ph,i}(t)$, proportional to the current intensity values.

### 2.2. Experimental set-up

Once the hardware components of the lab-replica were established, as a first step, a mathematical model was developed to correlate the applied input voltage to the resulting beam-spot position on the oscilloscope. Although such a model is not strictly required for implementing a PID controller, it provides a valuable framework for simulating the process dynamics, also enabling systematic controller tuning. To achieve this, two tests were designed-referred to as static analysis and transient analysis, both developed using the open-loop scheme shown in Fig. 3. For conducting these tests and for subsequent control implementation, the STM32 NUCLEO-H723ZG microcontroller was selected. Among its key features, this microcontroller integrates an ARM Cortex-M7 core operating at 550 $MHz$ with a floating-point unit, 512 $KB$ of flash memory, 564 $KB$ of SRAM, and six SPI interfaces, providing high performance in terms of computational velocity, data transmission, and storage capacity. A key advantage of this microcontroller is the presence of two independent 12-bit Digital-to-Analog Converters (DACs), which, in this specific application, were used to control the movement of the oscilloscope spot. This was accomplished by connecting the voltage outputs, $V_x$ and $V_y$, directly to the oscilloscope probes. The spot position was then detected by the sensor attached to the oscilloscope screen. The sensor, based on the intensity of incident light, generated four distinct currents, which were subsequently measured by the picoammeter and transmitted to a computer for further processing. To synchronize the data from the picoammeter with the $V_x$ and $V_y$ outputs of the microcontroller, a trigger was employed, establishing a connection between the two devices.

### 2.3. Steady-state analysis

The purpose of the steady-state analysis was to determine the relationship between the oscilloscope input voltages $V_x$ and $V_y$ (the process input signal) and the position $P_x$ and $P_y$ (the process output signal) of the spot visible on the oscilloscope screen, in order to derive the steady-state characteristic curve of the model.

During the steady-state analysis, an area of $3.3\ mm \times 3.8\ mm$ related to the oscilloscope screen was spanned, according to the path shown in Fig. 4(a). To minimize the data volume while preserving the essential information for curve reconstruction, the area was discretized into $n_x = n_y = 205$ levels along both axes, mapped to voltage values in the range 0 to 3.3 V, resulting in a voltage increment of:

$$V_{level} = \frac{V_{range}}{n} = \frac{3.3V}{205} \approx 16mV \tag{1}$$

These voltage levels were sent to the oscilloscope probes using the two STM32 DACs managed within an algorithm on the microcontroller, causing the change in position of the spot. In each calculation loop, the DACs value is increased by a fixed digital increment equal to $V_{bit} = 20$. To ensure synchronization between the applied voltages and the resulting change in position, the acquisition was carried out using each voltage level as a trigger signal. The results of the steady-state analysis are shown in Figs. 4 and 5.

In particular, Fig. 4(c) illustrates the normalized currents generated by the four quadrants of the BPM sensor during the spanning test. Each current signal is normalized with respect to the total current, according to

$$\bar{I}_{ph,i}(t) = \frac{I_{ph,i}(t)}{\sum_{i=1}^{4} I_{ph,i}(t)} \tag{2}$$

where $i = 1, \ldots, 4$ denotes the $ith$ quadrant of the optical sensor. This normalization mitigates the effect of external disturbances such as

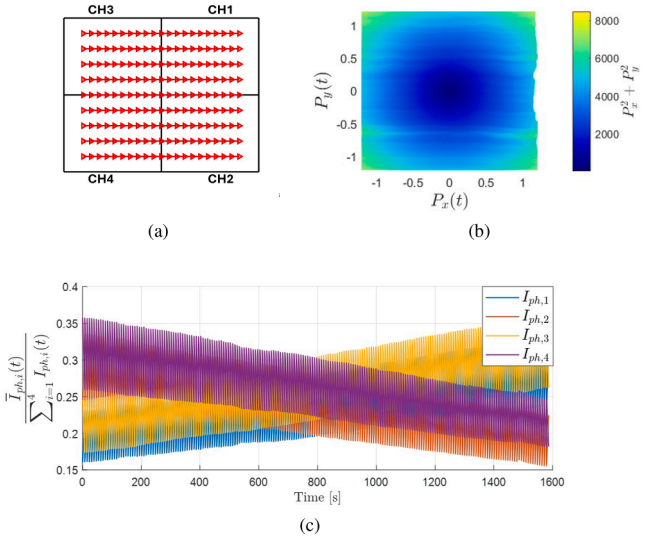


**Fig. 4.** (a) Path of the oscilloscope spot during the steady-state analysis; in black are shown the edges of the optic sensor quadrants during the test, where the spot was moved inside this region. (b) Spot's centering, based on the current values measured by the sensor. (c) Evolution of the normalized currents during the test. (For interpretation of the references to color in this figure legend, the reader is referred to the web version of this article.)

ambient light fluctuations, while also compensating for variations in the overall beam intensity. The normalized currents exhibit the expected complementary behavior: the currents from the lower quadrants (red, purple) decrease as the spot moves upward, whereas those from the upper quadrants (yellow, blue) increase. Finally, the intersection of the currents corresponds to the spot crossing the vertical midline of the sensor, which corresponds to the center location of the four quadrants.

Knowing the four currents, the horizontal ($P_x$) and vertical ($P_y$) position of the spot were obtained using the following equations:

$$P_x(t) = k_x \cdot \frac{(I_{ph,1}(t) + I_{ph,2}(t)) - (I_{ph,3}(t) + I_{ph,4}(t))}{\sum_{i=1}^{4} I_{ph,i}(t)} \tag{3}$$

$$P_y(t) = k_y \cdot \frac{(I_{ph,1}(t) + I_{ph,3}(t)) - (I_{ph,2}(t) + I_{ph,4}(t))}{\sum_{i=1}^{4} I_{ph,i}(t)} \tag{4}$$

where $k_x$ and $k_y$ represent the conversion factors used to express the positions in a specific unit of measurement, in this case, millimeters. To obtain the values of these parameters, they were initially set to 1. Subsequently, the minimum and maximum values of the positions along the two axes were computed and compared with the corresponding real measured values. At this stage, the values of $k_x$ and $k_y$ were calculated as:

$$k_x = \frac{P^{max}_{x,real} - P^{min}_{x,real}}{P^{max}_{x,k=1} - P^{min}_{x,k=1}} = 9.9586\ mm \tag{5}$$

$$k_y = \frac{P^{max}_{y,real} - P^{min}_{y,real}}{P^{max}_{y,k=1} - P^{min}_{y,k=1}} = 9.8306\ mm \tag{6}$$

In Fig. 4(a) it was verified that the sensor operates correctly, as the quadratic sum of $P_x$ and $P_y$, represented in the colormap, reaches its minimum value at the point (0,0), which corresponds to the center of the sensor. From Fig. 5(a) it is shown that the position along the $y$-axis remains unchanged during the displacement along the $x$-axis, with only slight variation induced by ambient light fluctuations. This observation is crucial because it allows to decouple the two variables, considering each position independently. Therefore, since the two control variables, the $x$ and $y$ positions of the beam, can be treated as independent, the

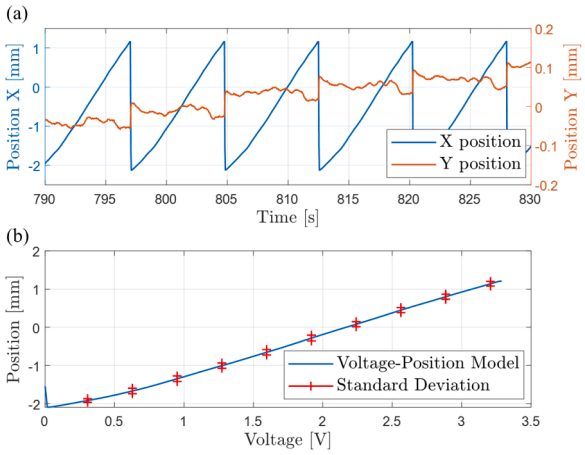


**Fig. 5.** (a) Computed trajectories of the $X$ and $Y$ positions, confirming the absence of cross-coupling effects and allowing the system to be modeled as two independent Single-Input Single-Output (SISO) systems. (b) Steady-state Voltage–Position characteristic curve, demonstrating linear behavior across the full operating range.

study will focus exclusively on the control of a single axis, specifically the $x$-axis.

By dividing the entire dataset into $n_y$ curves, each representing the evolution of the beam's $x$-position at a fixed $y$-coordinate, analytically described as

$$\overline{P}_x^{(k)} = \{ P_x(t) \mid P_y(t) = y_k \}\ ,\ k = 1, 2, \dots, n_y. \tag{7}$$

the steady-state voltage–position characteristic along the $x$-axis can be reconstructed. Specifically, for each voltage level $i$ along the $x$-axis, the mean $\bar{\mu}_x(i)$ and standard deviation $\bar{\sigma}_x(i)$ across the different $n_y$ curves are computed as

$$\bar{\mu}_x(i) = \frac{1}{n_y} \sum_{k=1}^{n_y} \overline{P}_x^{(k)}(i) \tag{8}$$

$$\bar{\sigma}_x(i) = \sqrt{\frac{1}{n_y - 1} \sum_{k=1}^{n_y} (\overline{P}_x^{(k)}(i) - \bar{\mu}_x(i))^2} \tag{9}$$

The resulting characteristic curve is then expressed as the interpolation of the resulting $\bar{\mu}_x(i)$

$$X(i) = \bar{\mu}_x(i) \pm \bar{\sigma}_x(i) \tag{10}$$

with $i$ representing the sample associated with the $ith$ voltage level along the $x$-axis. In Fig. 5(b), the resulting characteristic curve $X(i)$ is shown, illustrating the behavior of the spot along $x$ and its variability across the different $y$-positions. It can be observed that the characteristic curve does not exhibit saturation at the extremes but remains linear throughout the entire voltage range.

### 2.4. Transient analysis

The second test aimed at identifying the dynamical model of the system was the transient analysis. The purpose of this analysis was to measure the evolution of the process during a step response in order to identify its dynamics. This dynamics depends on the bandwidth of the connected equipment and their respective latencies. Specifically, the dominant bandwidth is determined by the picoammeter, which, within the current range of $\pm 2.5\ \mu A$, has a bandwidth of approximately $700\ Hz$. In more detail, the test was carried out by measuring the evolution of the spot position along the $x$-axis following a voltage step input.

The voltage input was supplied by an STM32 DAC, programmed to transition from $0\ V$ to $3.3\ V$ after $0.04\ s$, causing the spot to move along the $x$-axis. To optimize data processing, current values, sampled at a

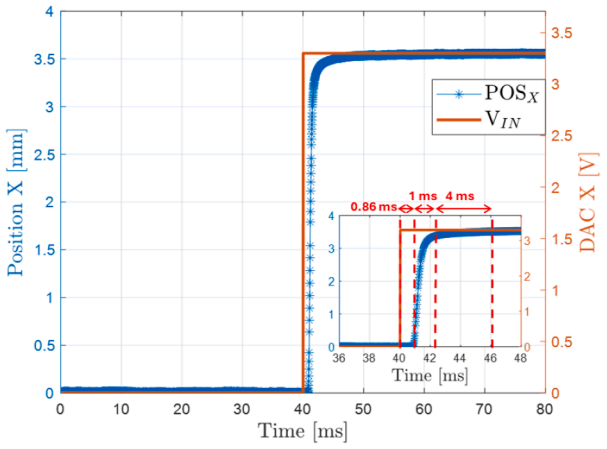


**Fig. 6.** Spot position along the $x$-axis with respect to the applied voltage step. Despite the rapid dynamics, the position exhibits a transient phase lasting approximately 5 $ms$. Within this period, the first $ms$ corresponds to the actual displacement of the spot, while the remaining time accounts for the evolution of its intensity before reaching a steady value. Additionally, the graph reveals the presence of a latency between the voltage input and the onset of the system's response, measured at approximately 0.86 $ms$.

frequency of 54 $kHz$, were stored in a buffer with a capacity of 5,000 entries. Once the buffer was filled, the data were saved and processed to compute the spot positions.

The results of the transient analysis are presented in Fig. 6, where the blue line represents the spot $x$-position evolution, while the red line corresponds to the step voltage applied to the oscilloscope. From this graph, it is possible to identify the transfer function of the system using a first-order dynamical model approximation with delay (Bolzern et al., 2008), considering that the response does not exhibit overshoot. The generic associated transfer function is:

$$P(s) = \frac{K}{1+Ts} e^{-\tau s} \tag{11}$$

where $K$ represents the system gain, $T$ is the equivalent time constant, and $\tau$ denotes the *equivalent delay*. The identification of these parameters was performed by applying the area method. This technique is commonly used to determine the parameters of the approximated model described in Eq. (11), based on the system's experimental step response. The final transfer function that identifies the open-loop model is the following.

$$P(s) = \frac{1.076}{1 + 4.79 \cdot 10^{-4} s} e^{-8.6 \cdot 10^{-4} s} \tag{12}$$

Within the validation framework, model accuracy was quantified by comparing the measured dataset ($y$) with the identified open-loop response ($\hat{y}$) shown in Fig. 7, using the percent fit (FIT%), the root mean square error (RMSE%), and the variance accounted for (VAF). The evaluation resulted in the following values:

$$FIT\% = 100 \cdot \left(1 - \frac{\|y - \hat{y}\|_2}{\|y - \bar{y}\|_2}\right) = 91.9\% \tag{13}$$

$$RMSE\% = \sqrt{\frac{1}{N} \cdot \sum_{i=1}^{N} (y_i - \hat{y}_i)^2} \cdot \frac{100}{y_{max} - y_{min}} = 1.04\% \tag{14}$$

$$VAF\% = 100 \cdot \left[1 - \frac{var(y - \hat{y})}{var(y)}\right] = 99.3\% \tag{15}$$

where $\bar{y}$ is the mean value of the real transient analysis dataset, and the $var$ operator indicates the variance. The obtained values of FIT (91.9%), RMSE% (1.04%) and VAF (99.3%) demonstrate a satisfactory level of agreement between the model and the experimental data, thereby validating the model's adequacy and its applicability to the subsequent PID controller design.

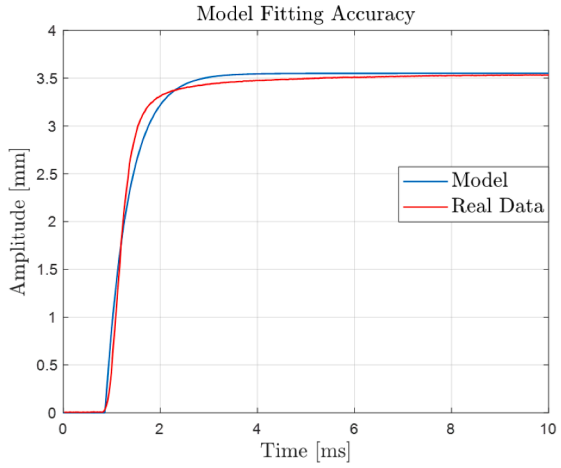


**Fig. 7.** Comparison of the model and the experimental step response.

## 3. Control strategy

To ensure consistency with the state-of-the-art and facilitate deployment on a real system, a PI controller was designed, characterized by the following transfer function:

$$C(s) = K_p \cdot \left(1 + \frac{1}{T_i s}\right) \tag{16}$$

where $K_p$ is the proportional gain, and $T_i$ is the integral (or reset) time. The derivative term was not included in the controller design because the BPM sensor employed is not visible-blind and is thus subject to ambient light fluctuations. In fact, the derivative action is particularly sensitive to noise on the measurement signal; its use could introduce instability. Given the previously estimated open-loop transfer function, to find the optimal PI parameters, two open-loop tuning methods were applied and compared, namely the *Ziegler-Nichols* and *Cohen-Coon* open-loop methods (Bolzern et al., 2008), selected as representative and widely validated approaches in classical control design. The purpose of introducing both methods was to provide two representative tuning methods and demonstrate the differences in their performances in both simulation and experimental world. Both techniques define the design of the parameters for a Proportional (P), Proportional-Integral (PI) or Proportional-Integral-Derivative (PID) controller based on the characteristic values of the open-loop transfer function. According to the Ziegler-Nichols open-loop method, the proportional gain $K_p$ and the integral time $T_i$ for a PI controller are given by:

$$K_p = \frac{0.9T}{K\tau} \qquad T_i = 3\tau \tag{17}$$

Similarly, the Cohen-Coon method provides the following expressions:

$$K_p = \frac{10.8T + \tau}{12K\tau} \qquad T_i = \tau \frac{30T + 30\tau}{9T + 20\tau} \tag{18}$$

By substituting the values of $T$, $\tau$, and $K$ as defined in Eq. (11), and considering a PI controller, the values of $K_p$ and $T_i$ given in Eq. (16) are obtained. The associated transfer functions are described as follows

$$C_{Zieg-Nich}(s) = 0.46576 \cdot \left(1 + \frac{1}{2.6 \cdot 10^{-3} s}\right) \tag{19}$$

$$C_{Coh-Coo}(s) = 0.54322 \cdot \left(1 + \frac{1}{6.78 \cdot 10^{-4} s}\right) \tag{20}$$

The closed-loop transfer functions were calculated to analyze the performance of the obtained controllers. In particular, by simulating a step input, the controller's action must drive the system to steady-state (reference) while optimizing key performance metrics such as rise time, overshoot, and steady-state error.

$$G_{Zieg-Nich}(s) = \frac{C_{Zieg-Nich}(s)P(s)}{1 + C_{Zieg-Nich}(s)P(s)} \tag{21}$$

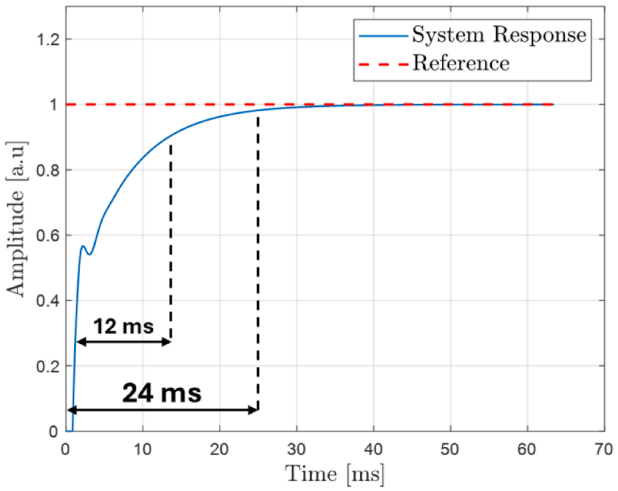


(a)

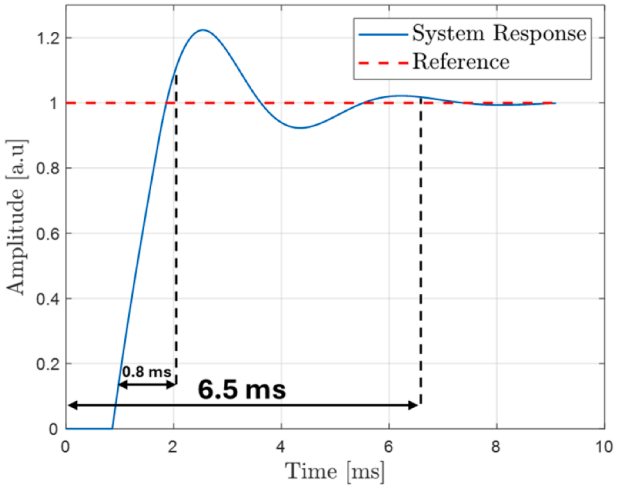


(b)

**Fig. 8.** Simulation of the closed-loop system's step response using the optimal PI parameters. The system response in (a) exhibits a rise time equal to 12 $ms$, with no overshoot, and a settling time of 24 $ms$. The system response in (b) shows instead a rise time equal to 0.8 $ms$, with an initial overshoot equal to 22% above the reference, and a settling time equal to 6.5 $ms$.

$$G_{Coh-Coo}(s) = \frac{C_{Coh-Coo}(s)P(s)}{1 + C_{Coh-Coo}(s)P(s)} \tag{22}$$

The results of the closed-loop system's step response are shown in Fig. 8. Both sets of PI parameters successfully stabilize the system. For Ziegler-Nichols, the gains are ($K_p = 0.46576$ and $K_i = 179.1$), resulting in a slower, smoother response without overshoot. The Cohen-Coon open-loop method yields higher gains ($K_p = 0.54322$ and $K_i = 801.2$), producing a faster response with slight overshoot and small oscillations around the reference before settling.

## 4. Experimental control system validation

To validate the control system, the hardware devices used for model identification were interconnected to form a closed-loop feedback system, as shown in Fig. 9. In this scheme, the control unit, i.e., the STM32 microcontroller, acts to convert the voltage signal obtained by the detection system into the equivalent spot position value. In particular, using

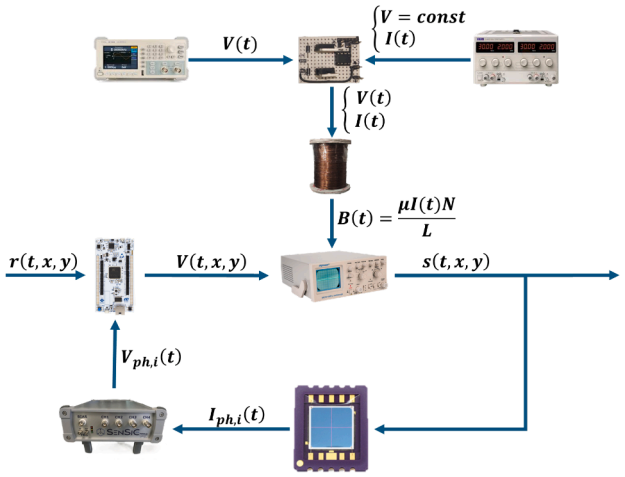


**Fig. 9.** Closed-loop control system architecture implemented during the experimental validation phase. Compared to the open-loop architecture, other devices were added to produce the disturbance acting on the beam, specifically a wave generator (top-left) and a power supply (top-right), which are connected to an electronic circuit, made by an operational amplifier in voltage follower configuration, to supply the signal $V(t)$ to follow and the current $I(t)$ required from the electromagnet.

Eqs. (3) and (4), $P_x$ and $P_y$ are evaluated, and the error $e(t, x, y)$ with respect to the reference is computed. Based on that error value, the microcontroller calculates the control voltage signal $V(t, x, y)$ through the PI control law, leading to the closure of the feedback loop. Consequently, this enables the system to autonomously regulate itself and effectively adapt to dynamic changes over time. The control-loop frequency depends on the hardware of the setup. Specifically, the analog bandwidth of the Front-End (FE) and the latency introduced by the Analog-to-Digital Converter (ADC) system limit the maximum achievable control-loop frequency to 500 $Hz$. Although the STM32 microcontroller is capable of operating at frequencies well into the tens of $kHz$ range, based on these constraints, we chose to set the control-loop frequency at 100 $Hz$. This conservative approach was made to ensure stability and reliability during the first experimental implementation, while still effectively compensating for slow drifts (such as those encountered in XAS experiments) and disturbances in the low-frequency range, which strongly affect real measurements.

### 4.1. PI tuning

The control performances with the PI gains obtained in simulation are shown in Fig. 10. In this case, the test was conducted by controlling the spot to move toward the zero reference, starting from an initial condition far from the target, and applying the control after one second. Although both controllers are stable in simulation, their behavior differs significantly when implemented in the real experimental context, so much so the CC-tuned controller becomes unstable. This instability is attributed to the higher integral gain associated with the CC tuning, which reduces robustness margins in the presence of unmodeled dynamics and non-idealities of the real system. These include discrete-time implementation effects, loop latency introduced by the ADC and communication chain, measurement noise, and deviations of the real plant from the simplified FOPDT model. Under these conditions, the CC tuning leads to a loss of stability, while the ZN tuning remains only marginally stable and exhibits oscillatory behavior. For these reasons, a tuning phase was necessary, involving multiple tests with different $K_p$ and $K_i$ values to determine the optimal parameters for the given case with a control frequency of 100 $Hz$. Since the initial values obtained from the calibration methods led to a system that was either marginally stable or outright

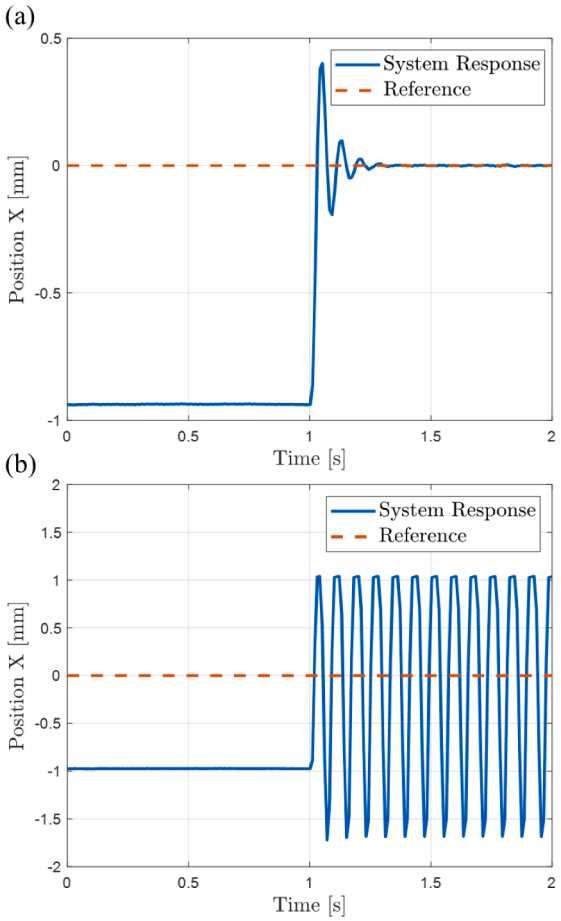


**Fig. 10.** Experimental closed-loop system response using the optimal PI parameters found with the Ziegler-Nichols and Cohen-Coon methods. In (a), it is shown that the system with the Ziegler-Nichols parameters is asymptotically stable, despite oscillatory behavior, while in (b), using the Cohen-Coon parameters, the system becomes unstable.

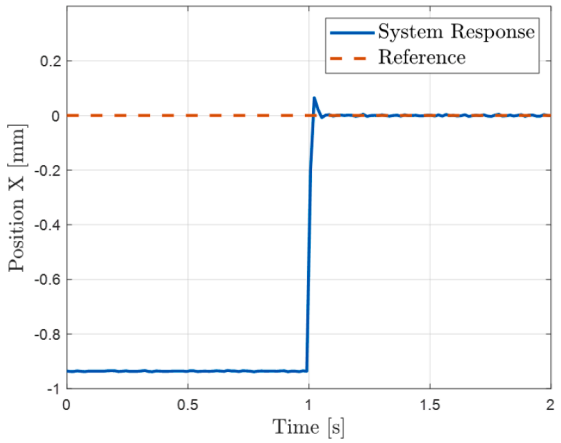


**Fig. 11.** Experimental closed-loop system response obtained using the optimal PI parameters identified during the tuning phase.

unstable, it was decided to start with lower proportional and integral gains. The most representative test results are summarized in Table 1.

It can be observed that in all stable tests, the integral action of the controller effectively reduces the steady-state error to near elimination. Selecting the closed-loop rise time and settling time as performance criteria, the optimal gains were identified as:

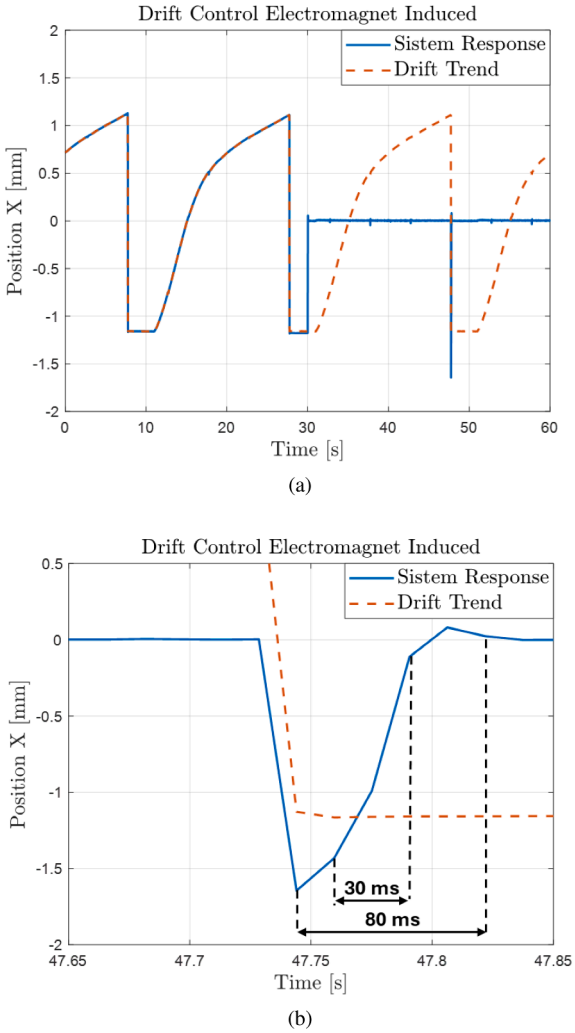


**Fig. 12.** Closed loop control system results in the presence of a position drift disturbance. In (a) the whole 60 $s$ experiment is shown, while in (b) a zoom of the peak, occurring around the 48th second of the experiment, is shown to underline the system's robustness against faster disturbances.

$$K_p = 2 \;;\; K_i = 215 \tag{23}$$

The closed-loop system response associated with these values is shown in Fig. 11. Although an error of 3 micrometers may seem excessive for modern synchrotrons, it is important to note that, in the experimental tests conducted, this corresponds to less than 0.4 % of the total displacement.

### 4.2. Position control with disturbance

The final step in validating the control system is assessing its disturbance rejection capability. In beamlines, one of the most significant disturbances is thermal drift, caused by temperature variations throughout the day. Since experiments in beamlines can last several hours, this disturbance can have a substantial impact on the overall experimental outcome. A particular example of an experiment highly affected by this phenomenon is the XAS. To simulate the disturbance to be compensated, an electromagnet was placed on top of the oscilloscope casing and powered by a signal generator producing a ramp signal with a frequency of 0.05 $Hz$ and a peak-to-peak voltage of 8 $V$. To observe the position variation of the spot caused by the electromagnet, the control algorithm was activated after 30$s$.

**Table 1**
PID tuning tests. Tests $N^o$ 1 and 2 correspond to the proportional and integral gains identified using the Ziegler-Nichols and Cohen-Coon open-loop methods discussed in Section 3. The subsequent tests were carried out by varying $K_p$ and $K_i$ around these sub-optimal values to assess their effect on the closed-loop performance.

| $N^o$ | $K_p$ | $K_i$ | Steady-State Error [$\mu m$] | Over shoot [%] | Rise Time [$ms$] | Settling Time (2%) [$ms$] |
|---|---|---|---|---|---|---|
| 1 | 0.46 | 180 | 3.14 | 40.4 | 10 | 72 |
| 2 | 0.54 | 801 | / | 109 | 10 | / |
| 3 | 0.05 | 50 | 3.63 | / | 280 | 650 |
| 4 | 0.05 | 75 | 3.25 | 3.9 | 46 | 145 |
| 5 | 0.05 | 100 | 3.38 | 120.75 | 13 | 163 |
| 6 | 0.05 | 215 | / | 64.33 | 12 | / |
| 7 | 0.1 | 75 | 2.45 | 3.31 | 46 | 148 |
| 8 | 1 | 215 | 2.89 | 37.41 | 15 | 157 |
| 9 | 2 | 215 | 2.77 | 6.37 | 15 | 68 |
| 10 | 3 | 215 | 2.61 | 24.02 | 12 | 301 |

The results are shown in Fig. 12. During the first 30 $s$ of the experiment, before the control algorithm is activated, the drift induced by the magnetic field generated by the electromagnet deflects the spot, initially positioned near zero, within a range from $-1.13$ $mm$ to 1.16 $mm$, with a slope of 0.11 $mm/s$.

Despite the electromagnet being driven by a ramp voltage, the resulting displacement does not follow the same trend. This is because the current, due to parasitic capacitive effects and non-idealities of the device, does not vary linearly with the applied voltage. The saturation effect observed at the minimum peak is instead attributed to the fact that a threshold magnetic field-and consequently a threshold current-must be exceeded to induce spot deflection. Once the control is activated, after 30 $s$, the system's response no longer follows the drift trend, as the PI controller actively corrects the spot's position toward the reference-the center of the screen-considered as zero. Another source of disturbance in the system is the abrupt position shift from its maximum to its minimum value, occurring at the end of each ramp period. This disturbance can be interpreted as a step change since, once the minimum value is reached, the drift remains constant until the magnetic field threshold required to deflect the spot is exceeded. Even in this case, the controller effectively compensates for the disturbance, achieving a rise time of 30 $ms$ and a settling time of approximately 80 $ms$.

## 5. Conclusions and outlook

This paper presented the development and experimental validation of an electrical actuation-based control system for stabilizing synchrotron X-ray beams. The key achievements of the control algorithm include the successful implementation of a laboratory-scale replica using an analog oscilloscope to simulate electron beam dynamics, allowing for the testing and validation of the control strategy in a lab-scale test environment. The steady-state and transient analyses provided a comprehensive understanding of the system's behavior, revealing a linear relationship between input voltages and beam position. Based on these analyses, the system was modeled as a first-order system with a delay, primarily attributed to the latency of the Analog-to-Digital Converter (ADC) within the picoammeter, and a PI control strategy was proposed and validated, demonstrating robust performance in maintaining beam stability even in the presence of disturbances.

The PI controller was tuned using both Ziegler-Nichols and Cohen-Coon methods, with experimental validation revealing the need for further adjustments to ensure stability under real-world constraints. The final optimized PI gains ($K_p = 2$, $K_i = 215$), obtained at 100 $Hz$ of control frequency, ensured excellent performance of the closed-loop system's response in terms of rise time, settling time, and steady-state error, with the system effectively compensating for disturbances such as thermal drift and abrupt position shifts. The successful implementation of the PI control strategy highlights its potential to improve the performance and reliability of synchrotron beamlines, contributing to more accurate and efficient scientific research and medical applications.

The proposed laboratory-scale replica constitutes a cost-effective and versatile platform for exploring beam stabilization strategies, enabling detailed investigation of system modeling, characterization, and control design within a simplified yet representative framework. When considering deployment in operational synchrotron facilities, the approach entails both opportunities and challenges. In particular, local electrical actuation on bending magnets has the potential to provide higher-bandwidth corrections directly at the beamline level, thereby enhancing beam stability beyond the limits typically achievable with optical actuators. Scaling to real facilities requires careful consideration of possible couplings in beam dynamics, as well as the impact of mechanical vibrations, electrical noise, and stringent safety requirements, so that local corrections do not interfere with the overall orbit stability. High-frequency noise sources, such as vibrations or power-supply ripple, often occur at well-defined frequencies and can be effectively identified and compensated by integrating a Proportional-Resonant (PR) controller alongside the PI controller, allowing targeted suppression of these disturbances. By upgrading the readout chain with faster and lower-latency electronics, the proposed control strategy could be extended to operate at higher loop frequencies, thereby offering a feasible and effective solution toward implementation in real synchrotron applications.

## CRediT authorship contribution statement

**Niccolò La Rosa:** Writing – review & editing, Writing – original draft, Visualization, Validation, Software, Resources, Methodology, Investigation, Formal analysis, Data curation, Conceptualization; **Samuele Moscato:** Writing – review & editing, Validation, Supervision, Software, Methodology, Investigation, Formal analysis, Data curation, Conceptualization; **Luigi Fortuna:** Writing – review & editing, Supervision, Methodology, Conceptualization; **Maide Bucolo:** Writing – review & editing, Visualization, Validation, Supervision, Resources, Project administration, Methodology, Funding acquisition, Data curation, Conceptualization; **Massimo Camarda:** Writing – review & editing, Validation, Supervision, Resources, Project administration, Methodology, Investigation, Funding acquisition, Formal analysis, Data curation, Conceptualization.

## Declaration of competing interest

The authors declare the following financial interests/personal relationships which may be considered as potential competing interests: The PhD scholarship, held by the first author of the paper, is sponsored by the company STLab s.r.l. The system developed as part of this research is intended to be commercialized by the company at a later stage. All results have been collected and analyzed in accordance with the FAIR data principles and have been fully disclosed to ensure transparent evaluation.

## Funding information

This research was partially supported by the SAMOTHRACE project (Avviso 'SAMOTHRACE' ECS00000022-CUP B63D21015260004). This project has received funding from the European Union's Horizon 2020 research and innovation program under grant agreement No 101007417, within the framework of the NFFA-Europe Pilot Transnational Access Activity, proposal ID738.

## References

Alcock, S. G., Nistea, I., Sutter, J. P., Owen, R. L., Axford, D., Foster, A., Sawhney, K., & Signorato, R. (2018). Developing bimorph mirrors into rapidly deformable active optics for synchrotron X-ray beamlines. In *Imaging and applied optics 2018 (3d, AO, AIO, COSI, DH, IS, LACSEA, LS&c, MATH, pc1842AOP)* (p. OW2J.2). Optica Publishing Group. https://doi.org/10.1364/AOMS.2018.OW2J.2

Bai, Y., Gong, X., Lu, Q., Li, S., Song, Y., Peng, Z., & Zhang, Z. (2023). Research on an active control method of double crystal monochromator with disturbance observer. *Nuclear Instruments and Methods in Physics Research Section A: Accelerators, Spectrometers, Detectors and Associated Equipment*, *1057*, 168729. https://doi.org/10.1016/j.nima.2023.168729

Bloomer, C., & Rehm, G. (2016). The use of single-crystal CVD diamond X-ray beam diagnostics for synchrotron beamline commissioning and operation at diamond light source ltd. *2016 IEEE Nuclear Science Symposium, Medical Imaging Conference and Room-Temperature Semiconductor Detector Workshop (NSS/MIC/RTSD)*, (pp. 1–7). https://doi.org/10.1109/NSSMIC.2016.8069893

Bloomer, C., Rehm, G., & Tipper, A. (2019). Fast feedback using electron beam steering to maintain the X-ray beam position at a monochromatic X-ray diagnostic at diamond light source. In *Proc. IBIC'19* number 8 in International Beam Instrumentation Conferenc (pp. 172–176). JACoW Publishing, Geneva, Switzerland. https://doi.org/10.18429/JACoW-IBIC2019-MOPP032

Bolzern, P., Scattolini, R., Schiavoni, N. et al. (2008). Fondamenti di controlli automatici. McGraw-Hill.

ELS, C. (2025). B.E.S.T. https://www.caenels.com/product/best/.

Engblom, C., Alves, F., Blache, F., Corruble, D., Dawiec, A., Diop, M., Hubert, N., Kubsky, S., Langlois, F., Marchand, P. et al. (2016). Overview of some feedback-& control system at synchrotron SOLEIL. In *The 11th international workshop on personal computers and particle accelerator controls (PCaPAC), Brazil*.

Fan, C., & Zhao, Z. (2018). Synchrotron radiation in materials science: light sources, techniques, and applications. John Wiley & Sons.

Forck, P., Liakin, D., & Kowina, P. (2009). Beam position monitors. In *CERN Accelerator School: Beam Diagnostics* (Dourdan, France, 28 May–6 June), pp. 187–228. CERN.

Huang, L., Xue, J., & Idir, M. (2016). Control x-ray deformable mirrors with few measurements. In S. L. O'Dell, & A. M. Khounsary (Eds.), *Adaptive x-ray optics IV* (p. 99650H). International Society for Optics and Photonics SPIE (*vol. 9965*). https://doi.org/10.1117/12.2237808

Huang, X. Y., Jiao, Y., & Wei, Y. (2021). Preliminary investigation of the noises and updates on physics studies of FOFB in HEPS. In *Proc. IPAC'21* number 12 in International Particle Accelerator Conference (pp. 2197–2199). JACoW Publishing, Geneva, Switzerland. https://doi.org/10.18429/JACoW-IPAC2021-TUPAB304

Hubert, N., Cassinari, L., Denard, J. C., Filhol, J. M., Leclercq, N., Nadji, A., Nadolski, L., & Pédeau, D. (2016). Commissioning of SOLEIL fast orbit feedback system. In *Epac* (pp. 3248–3250). (*vol. 8*).

Hubert, N., Cassinari, L., Denard, J. C., Nadji, A., & Nadolski, L. (2009). Global orbit feedback systems down to DC using fast and slow correctors. In *Proceedings of DIPAC 2009* (Basel, Switzerland), pp. 27–31. PSI.

Jiang, Z., Jiang, H., He, Y., He, Y., Liang, D., Yu, H., Li, A., & Signorato, R. (2025). Development and testing of a dual-frequency real-time hardware feedback system for the hard X-ray nanoprobe beamline of the SSRF. *Journal of Synchrotron Radiation*, *32*(1), 100–108. https://doi.org/10.1107/S1600577524010208

Kongtawong, S., Tian, Y., Yang, X., Ha, K., Yu, L. H., & Shaftan, T. (2020). Recent improvements in beam orbit feedback at NSLS-II. *Nuclear Instruments and Methods in Physics Research Section A: Accelerators, Spectrometers, Detectors and Associated Equipment*, *976*, 164250. https://doi.org/10.1016/j.nima.2020.164250

Möller, S. (2020). Accelerator technology. Springer Cham. https://doi.org/10.1007/978-3-030-62308-1

Rehm, G. (2013). Achieving and measuring sub-micrometer beam stability at 3rd generation light sources. In *Journal of physics: Conference series* (p. 042001). IOP Publishing (*vol. 425*).

Schneider, D. K., Shi, W., Andi, B., Jakoncic, J., Gao, Y., Bhogadi, D. K., Myers, S. F., Martins, B., Skinner, J. M., Aishima, J., Qian, K., Bernstein, H. J., Lazo, E. O., Langdon, T., Lara, J., Shea-McCarthy, G., Idir, M., Huang, L., Chubar, O., Sweet, R. M., Berman, L. E., McSweeney, S., & Fuchs, M. R., et al. (2021). FMX – the frontier microfocusing macromolecular crystallography beamline at the national synchrotron light source II. *Journal of Synchrotron Radiation*, *28*(2), 650–665. https://doi.org/10.1107/S1600577520016173

SenSic (2024). Electronic readout. https://www.sensic.ch/electronic-readout.

Tian, Y., Ha, K., Yu, L., Cheng, W., DeLong, J., Dalesio, L., & Levine, W. (2015). NSLS-II fast orbit feedback system. In *Proceedings of ICALEPCS2015 conference*.

Wang, X., Yan, Z. B., & Du, H. W. (2012). Suppression of ground vibration for SSRF foundation. In *Vibration, structural engineering and measurement i* (pp. 30–33). Trans Tech Publications Ltd (*vol. 105*). Applied Mechanics and Materials. https://doi.org/{10.4028/www.scientific.net/AMM.105-107.30}

Zhang, C., Liu, H., Wang, C., Guo, Z., Zhang, X., Xu, Z., Zhen, X., Wang, Y., & Tai, R. (2023). Automatic feedback system for x-ray flux at BL08U1A soft x-ray spectromicroscopy beamline of Shanghai synchrotron radiation facility. *Applied Sciences*, *13*(9). https://doi.org/10.3390/app13095456